Soft Matter

ROYAL SOCIETY OF CHEMISTRY

PAPER

View Article Online
View Journal | View Issue

Cite this: *Soft Matter*, 2026, **22**, 2447

Response to dynamic shape changes in suspensions of hard rectangles

Denis Dertli and Thomas Speck*

Received 13th January 2026,
Accepted 28th February 2026

DOI: 10.1039/d6sm00037a

rsc.li/soft-matter-journal

While the autonomous assembly of hard nanoparticles with different shapes has been studied extensively both in experiments and simulations, little is known about systems where particle shape can be dynamically altered. DNA origami nanostructures offer an alternative route to synthesize nanoparticles that can change their shape on demand. Motivated by recent experiments, here we study the structure and dynamics of suspensions of hard squares in response to an elongation into a rectangle. Performing dynamic hard-particle Monte Carlo simulations at constant volume and employing two protocols, we numerically analyze the collective diffusion and ordering during the shape change and the subsequent relaxation towards the new equilibrium state. We find that the cascading protocol, which mimics experimentally realized DNA origami, can become dynamically arrested due to the increase in effective packing fraction.

1 Introduction

The interactions between hard particles are determined by their excluded volume and their shape. While in the simplest case these are spheres,[1] colloidal and nanoparticles with different shapes can now be synthesized routinely.[2,3] In fact, through varying their shape an astonishingly wide range of ordered structures can be accessed in dense suspensions of hard particles,[4] which has been captured in theoretical approaches[5,6] and rationalized through the emergence of directed entropic forces.[7] In particular in two dimensions, there is a rich transition behavior in hard-particle systems governed by shape and symmetry.[8,9] Hard-particle Monte Carlo (MC) simulations have been successfully utilized in order to study the equilibrium phase behavior of hard disks,[10–12] *n*-gons,[8] and hard rectangles.[13]

However, typically colloidal particles are immutable after they have been synthesized with relatively few studies in which the particle shape has been changed dynamically.[14–16] While the response of dense suspensions to density and temperature sweeps and quenches has been studied extensively, little is known about the response to a ‘‘shape sweep’’.

DNA origami offers an alternative route to synthesize nanoparticles with almost arbitrary shapes.[17] Essentially, a long single-stranded DNA scaffold is folded into a predetermined two- or three-dimensional nanostructure through hybridizing the scaffold with short complementary staple strands, which direct the folding and stabilize the final complex.[18–20] Such DNA-based nanostructures are extensively researched motivated by their potential applications for therapy and drug delivery.[21–26] Experimental studies on square and rod-like DNA origami nanostructures on lipid bilayers suggest that these can effectively behave as independent hard particles governed by Brownian motion.[27,28]

One of the key features of DNA origami is the opportunity to program different shapes and to dynamically reconfigure particle shape through the addition of trigger strands[29–32] that are designed to be more complementary to parts of the origami structure than the original staple strands. The trigger strands bind to short, exposed single-stranded ‘‘toeholds’’, initiating a cascade where they displace the original staples and thus cause a conformational change in the origami. In particular, a step-by-step relay process from a square to a rectangular shape has been implemented.[30,31] This process has been exploited recently to achieve the reversible opening and closing of channels in synthetic cells due to collective forces exerted by the DNA nanostructures.[28] Inspired by these experiments (and others[33]), here we leverage computer simulations to study the collective behavior in suspensions of hard particles after triggering a change of their aspect ratio while keeping the area fixed. We compare two time-dependent protocols for the shape transformation and extend the established hard-particle MC simulation approach by incorporating these transformations: the cascading protocol following the experiments and a strongly simplified ‘‘morphing’’ protocol in which the initial squares are stretched over time [Fig. 1(a and b)]. Our numerical investigations focus on the diffusion and order properties in our many-particle systems. Both the dynamics during the shape change and the subsequent relaxation are addressed and compared to equilibrium.

2 Simulation details

We study a two-dimensional system of $N \simeq 1300$ particles with fixed area σ^2 at constant packing fraction ϕ and periodic

Institute for Theoretical Physics IV, University of Stuttgart, Heisenbergstr. 3, 70569 Stuttgart, Germany. E-mail: thomas.speck@itp4.uni-stuttgart.de

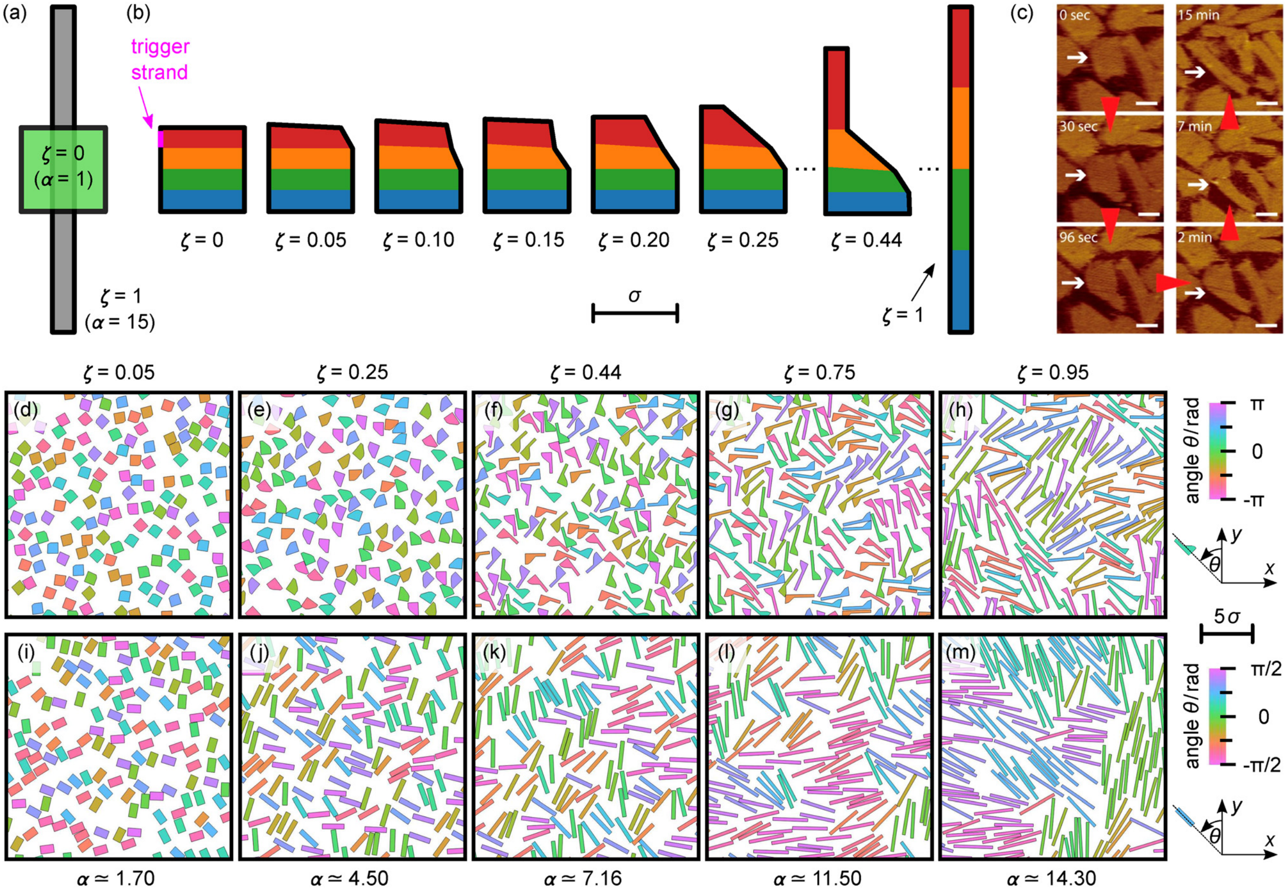

Fig. 1 Shape transformation protocols: (a) morphing and (b) cascading. For the latter, the shape is divided into four sub-polygons with constant area each. The magenta arrow indicates the trigger strand in the upper left segment. (c) AFM images of DNA origami showing the cascading shape change (reproduced with permission from ref. 31). (d)–(m) Simulation snapshots (showing excerpts of the full system) representing different stages of a shape sweep at packing fraction $\phi = 0.32$ for the (d)–(h) cascading and (i)–(m) morphing protocol. The colors indicate the orientation with respect to the y-axis.

boundary conditions.[34] A single configuration comprises the centroid positions $\mathbf{r}_k$ and the angles $\theta_k \in [-\pi/n,\pi/n)$ enclosed with the y-axis for each particle with n-fold rotational symmetry. Throughout, we employ dimensionless quantities with length unit σ.

The particles interact through their excluded volume and we perform hard-particle MC simulations utilizing HOOMD-blue.[35–38] Only small local trial moves for translation and rotation are used that are either accepted or rejected if they lead to an overlap. For details on the Metropolis scheme for hard shapes, see ref. 37.

In addition, we attempt shape changes. We consider two shape transformation protocols and introduce a shape parameter $\zeta \in [0,1]$ that tracks the actual shape: (i) the morphing protocol shown in Fig. 1(a), whereby the aspect ratio α of a rectangle is successively increased from $\alpha = 1$ ($\zeta = 0$) to $\alpha = 15$ ($\zeta = 1$), *i.e.*, $\zeta = (\alpha - 1)/14$ and (ii) the cascading protocol in Fig. 1(b) that also starts with a square shape ($\zeta = 0$) but captures some features of the toehold-mediated strand displacement process more accurately. During this protocol the outer particle shape is defined by a set of ten vertices that span four interior polygons [Fig. 1(b)]. The shape moves are designed to mimic the experimentally observed cascading DNA origami transformations[30,31] [Fig. 1(c)]. We suppose that the trigger strand corresponds to the left segment of the sub-polygon on the top. This segment starts to elongate, resulting in a deformation of the corresponding sub-polygon. Additionally, each sub-polygon is constrained to maintain a constant area $\sigma^2/4$. At $\zeta \simeq 0.44$, the sub-polygon on the top has reached its final shape. At the end of the cascading protocol ($\zeta = 1$), particles have become rectangles with aspect ratio $\alpha = 15$. For both protocols, a trial shape change is applied to all particles simultaneously and only accepted if no particle experiences an overlap so that the shape remains synchronous, *i.e.*, all particles exhibit the same value ζ. Attempted changes of ζ are very small ($\Delta\zeta \sim 10^{-6}$) and our simulations essentially probe the quasi-static limit.

Note that advancing the shape is irreversible and thus breaks detailed balance. In the experiments, triggering the cascade releases elastic energy stored within the DNA origamis, which we assume to be sufficiently large to drive the shape evolution predominantly in the forward direction so that the probability for a backward transition is vanishingly small. We approximate this behavior through an irreversible MC move. Because the shape changes are quasi-static, small, and applied uniformly, they minimally perturb the local dynamics.

Moreover, we identify one MC time step as one local translation/rotation trial move per particle, while shape-change attempts are not counted as MC time step. This choice is motivated by the strong separation of time scales between local translational/rotational diffusion and the overall shape transformation. The Brownian time associated with particle diffusion is $t_B \sim 10^{-1}$ ms (SI S6 and S7[39]), which is several orders of magnitudes smaller than the duration ∼10 min of the experimental DNA origami shape transformation process.[31] Our MC scheme therefore provides a physically motivated, directional driving of the system that captures the irreversible, stress-driven shape evolution observed in the experiments while preserving correct sampling of local particle dynamics.

Our simulations prepare equilibrated configurations at the target packing fraction. The shape transformation is triggered (defining $\tau = 0$) and we start collecting configurations. During this process, all particles either attempt local translation/rotation trial moves or a global small shape update advancing ζ. The simulation is run until either the target shape ($\zeta = 1$) is reached or "jamming" occurs, *i.e.*, further shape updates are accepted only very rarely (the acceptance ratio has dropped from initially one to below 10^{-6}). We then start the relaxation run (defining $\tau' = 0$), where we collect further configurations without shape updates. Note that the only difference between the MC time step τ (starts counting from the beginning of the shape sweep) and τ' (starts counting after the shape sweep or for the runs without shape changes once stationarity is reached) is the choice of the zero point that defines the reference frame for calculating the mean-square displacement below. If not stated otherwise, we calculate the mean $\langle\cdot\rangle$ obtained from $\lessapprox$ 30 simulation runs with different random number seeds. A detailed description of our simulation protocol is provided in the SI.[39]

MC moves do not necessarily reproduce Brownian dynamics (BD). A dynamical interpretation is justified when employing sufficiently small, local translation and rotation moves such that the stochastic evolution approaches the small-step diffusive limit and can be mapped onto overdamped Brownian motion on intermediate and long time scales. In this limit, one MC sweep (one translation/rotation trial move per particle) defines a time increment that can be consistently rescaled to physical time. One approach to achieve a quantitative correspondence between MC and BD simulations relies on the acceptance rates to rescale MC time to match the diffusion behavior.[40–44] Here we opt to match the long-time diffusion coefficients in the dilute limit between MC and BD simulations.

In order to approximately map the simulation time τ to "real" time t, we conduct numerical hydrodynamic calculations to obtain the single-particle diffusion coefficient D_0 for each shape considered.[45] To this end, each (rigid) shape is represented by a collection of beads. We use the programs HYDRO2D-Circles[46] for processing and HYDRO++ for the calculation of the hydrodynamic coefficients and other solution properties.[47–50] Note that the hydrodynamic calculations are consistent with BD simulations (SI S6[39]). With the shape-independent effective diffusion coefficient $D_{\mathrm{eff},0}$ of the MC simulations at vanishing density, physical time increments are estimated as

$$\mathrm{d}t \sim \frac{D_{\mathrm{eff},0}}{D_0(\zeta(\tau))}\mathrm{d}\tau, \tag{1}$$

which we integrate along the protocols to obtain t. In the following, we express physical time in units of the Brownian time $t_B = \sigma^2/(4D_0)$ for a disk. Further details on the Brownian time rescaling for individual shapes can be found in the SI S5–S8.[39]

3 Results and discussion

3.1 Sweep of aspect ratio

For sweeps at low packing fraction ($\phi = 0.32$), the collective behavior within both protocols is shown in the sequences of simulation snapshots in Fig. 1. A crucial difference between the morphing and cascading protocols is that only during the morphing rectangles always exhibit a two-fold rotational symmetry and are space-filling. In total, we study five pairs of sweeps at different packing fractions shown within the phase diagram of hard rectangles in Fig. 2 that we obtained previously.[13] In equilibrium, hard rectangles exhibit four phases: isotropic fluid (I), nematic (N), smectic (S), and tetratic (T) order. While for sweeps at low packing fraction ($\phi < \phi_c$) the shape transformations always succeed (*i.e.*, $\zeta = 1$ reaches unity and particles have adopted the target shape), in the high packing fraction regime ($\phi > \phi_c$) we observe $\zeta = \zeta_f < 1$ for the cascading protocol. The distribution of the final shape

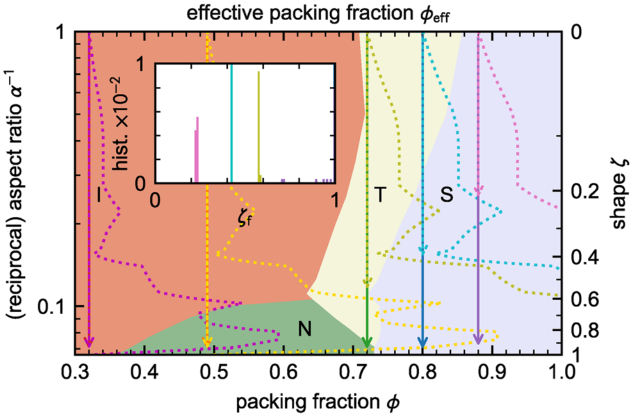

Fig. 2 Shape-changing protocols depicted in the phase diagram of hard rectangles. Five pairs of shape sweeps from $\alpha = 1$ (squares) to $\alpha = 15$ (rectangles) are investigated at packing fractions $\phi = 0.32$, 0.49, 0.72, 0.80 and 0.88. The solid and dotted arrows correspond to the morphing and cascading protocol, respectively. The transparent dotted curves show the effective packing fraction $\phi_{\mathrm{eff}}(\zeta)$ corresponding to the cascading protocol of the same color. For the morphing protocol this quantity coincides with the packing fraction ϕ. The underlying phase diagram is taken from ref. 13 comprising isotropic fluid (I), nematic (N), smectic (S), and tetratic (T) order. For the morphing protocol there is a direct correspondence from ζ (right axis) to aspect ratio α. The inset shows the distribution of the final shape parameter values ζ_f obtained from each simulation run. The target shape is reached ($\langle\zeta_f\rangle = 1$) except for: morphing protocol with $\phi = 0.88$ (purple) and cascading protocol with $\phi = 0.72$ (olive), 0.80 (cyan) and 0.88 (pink). Arrow heads terminate at $\langle\zeta_f\rangle$.

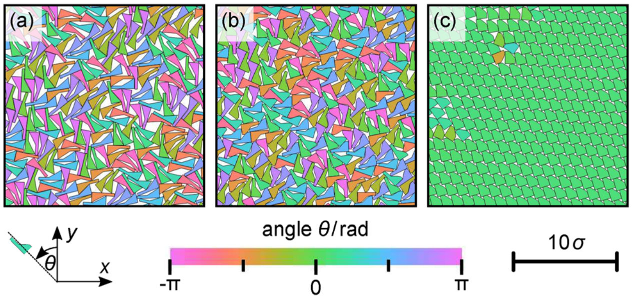

Fig. 3 Simulation snapshots (excerpts of the full system) showing the jamming ($\zeta \simeq \zeta_f \simeq$ const. < 1, $t/t_B \gtrsim 10^4$) observed at the termination of the shape change following the cascading protocol: (a) $\phi = 0.72$ ($\zeta_f \simeq 0.578$), (b) $\phi = 0.80$ ($\zeta_f \simeq 0.423$), and (c) $\phi = 0.88$ ($\zeta_f \simeq 0.233$).

parameter values ζ_f is very narrow as shown in the inset in Fig. 2. In Fig. 3, we show representative snapshots of configurations taken at the point when the final shape has been reached for the packing fractions where the final shape is not the target shape ($\zeta_f < 1$). For the morphing protocol at the highest packing fraction $\phi = 0.88$, a finite-size analysis[39] indicates that eventually $\zeta_f \to 1$ is reached. Interestingly, the sharp termination of the cascading protocol at values smaller than unity seem not to be subject to finite-size effects and occur at the same values of ζ_f independent of system size.

While the rectangles of the morphing protocol are always space-filling and the limit of unit maximal packing fraction can (in principle) be reached, for the intermediate non-space-filling shapes of the cascading protocol, the maximal packing fraction $\phi_{\max}(\zeta)$ is a nontrivial function of the shape parameter ζ. Here, we numerically estimate a lower bound for $\phi_{\max}(\zeta)$ from two close-packed antiparallel particles as illustrated in Fig. 4(a). The resulting maximal packing fraction is shown in Fig. 4(b). We identify the global minimum as the critical packing fraction $\phi_c \simeq 0.54$ above which completion of the cascading protocol can no longer be achieved. We use the maximal packing fraction $\phi_{\max}$ to rescale the prescribed constant packing fraction ϕ and define the effective packing fraction as $\phi_{\text{eff}}(\zeta) = \phi/\phi_{\max}(\zeta)$, which is plotted in Fig. 2. The effective packing fraction approaches its maximum of unity at the final shape parameter $\zeta_f < 1$ in the case of sweeps at high packing fraction. Accordingly, the dynamic arrest can be attributed to the effectively reduced space available during the cascading protocol.

3.2 Mean-square displacement

Our aim is to understand how a shape transformation impacts the average dynamics of particles. As reference, we first quantify the equilibrium diffusion coefficient D_{eff} obtained from the linear growth of the mean-square displacement (MSD) with respect to MC time τ through

$$r^2(\tau) = 2dD_{\text{eff}}\tau \tag{2}$$

in $d = 2$ dimensions. Given the trajectories $\{\mathbf{r}_k(\tau)\}_{k=1}^{N}$, we can calculate this quantity by exploiting both particle and time interval averages

$$r^2(\tau) = \left\langle \frac{1}{N}\sum_{k=1}^{N}\frac{1}{I_\tau}\sum_{i=0}^{I_\tau-1}[\mathbf{r}_k(\tau_i+\tau)-\mathbf{r}_k(\tau_i)]^2 \right\rangle \tag{3}$$

with the number $I_\tau = (\tau_f - \tau)/\Delta\tau + 1$ of time intervals of length τ, the sampled time points $\tau_i = i \times \Delta\tau$, the observation step size $\Delta\tau \simeq 10^4$, and the final MC time point $\tau_f \simeq 2 \times 10^8$. For calculating MSDs, we employ the package freud.[51]

Intuitively, we expect that higher packing fractions ϕ are associated with a slower growth of the MSD. This trend is confirmed by the motion of hard rectangles in Fig. 5(a). Another crucial impact on the available area to move is the shape of the particles as it defines the effectively excluded area. The reduced diffusion coefficients $D/D_0 = D_{\text{eff}}/D_{\text{eff},0}$ for different shapes (with the same area) are compared in Fig. 5(b). While the packing fraction is the dominant factor (approximately setting the order of magnitude), the shape leads to a "fine splitting" of the D/D_0 spectrum. One individual attribute of each shape is its circumference to ensure overall area equalization. Moreover, each shape possesses an individual degree of

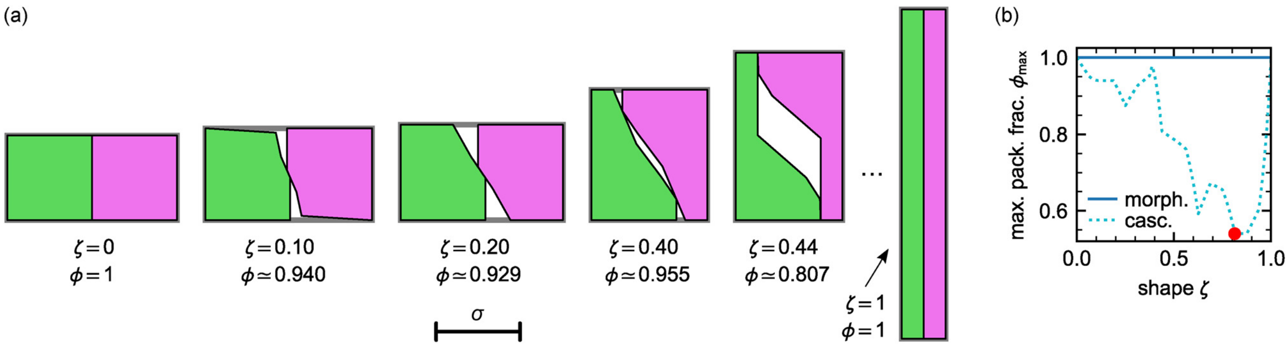

Fig. 4 Estimation of the maximal packing fraction. (a) Sequence of two close-packed antiparallel particles of the cascading protocol for different shape parameters ζ. The particles are enclosed by a box (gray), where we require that the vertical extension coincides with the length of the particles for the given ζ. For this simplified setup, we mimic the cascading behavior with small local moves by numerically minimizing the horizontal distance between the particles so that no overlap occurs and minimize the area A of the confining box. For the resulting configuration, we use the corresponding packing fraction $2\sigma^2/A$ as an estimate for (b) the maximal packing fraction $\phi_{\max}(\zeta)$ as a function of the shape parameter ζ for the morphing (solid blue constant) and cascading (dotted cyan curve) protocols. The red dot indicates the global minimum ($\zeta \simeq 0.813$, $\phi_c \simeq 0.54$).

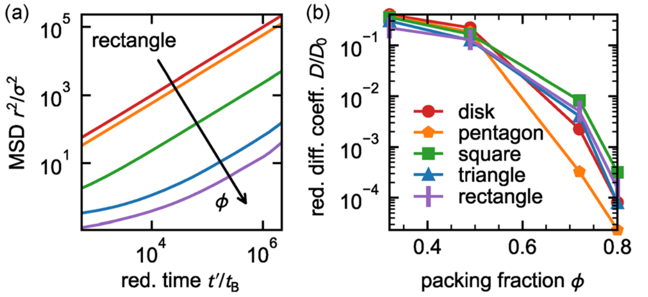

Fig. 5 Equilibrium diffusion behavior as function of packing fraction and shape. (a) MSD based on eqn (3) as a function of the reduced time t'/t_B for hard rectangles with aspect ratio $\alpha = 15$ at packing fractions $\phi = 0.32$ (red), 0.49 (orange), 0.72 (green), 0.80 (blue), and 0.88 (purple). (b) Long-time reduced diffusion coefficient D/D_0 for hard disks (red), pentagons (orange), squares (green), triangles (blue), and rectangles with aspect ratio $\alpha = 15$ (purple). The underlying D_{eff} have been estimated fitting the linear regime in (a) according to eqn (2) for the hard rectangles (and analogously for the other shapes[39]).

anisotropy with respect to rotational symmetry. For instance, shapes with an axial symmetry (*e.g.*, the rectangles) exhibit a further degree of freedom, allowing them to collectively align and reduce the excluded area cooperatively. Another fundamental aspect is the non-space-filling geometrical character of various shapes (*e.g.*, disks), *i.e.*, there is a maximal packing fraction above which an overlap-free configuration cannot exist anymore. The latter aspect is crucial at high packing fractions.

During the shape-changing protocols introduced in Section 2 and the subsequent relaxation, the MSD not only depends on the relative time difference but also the absolute time. For that reason, exploiting time averages as in eqn (3) is not feasible, and we have to adopt the definition of the MSD to

$$r^2(\tau) = \left\langle \frac{1}{N}\sum_{k=1}^{N}[\mathbf{r}_k(\tau) - \mathbf{r}_k(0)]^2 \right\rangle, \tag{4}$$

which can be formally understood as the special case of eqn (3) with a single time interval by interpreting $\tau = \tau_f$. Fig. 6 shows the evolution of the shape parameter ζ and the MSD, respectively, as a function of time during the five pairs of sweeps studied. In the low packing fraction regime ($\phi < \phi_c$), both protocols are in close accordance and show normal diffusion. The morphing protocol at the highest packing fraction $\phi = 0.88$ exhibits a slow evolution of shape but an apparently faster increase of the MSD than at $\phi = 0.80$, which can be attributed to the higher diffusion coefficient for squares. The inset in Fig. 6(b) zooms onto the evolution for $\phi = 0.49$, where we see a pronounced slow-down of the cascading dynamics before the target shape ($\zeta = 1$) is reached eventually (*cf.* the corresponding high effective packing fraction in Fig. 2). We find that $\phi = 0.49 < \phi_c$ is the highest investigated packing fraction for which a full completion of the cascading transformation ($\zeta = 1$) is achieved. At higher packing fractions ($\phi > \phi_c$), the cascading protocol does not recover from the slow-down and the dynamics is arrested, resulting in a flattening of shape [Fig. 6(a)] and MSD [Fig. 6(b)] curves converging to a constant value.

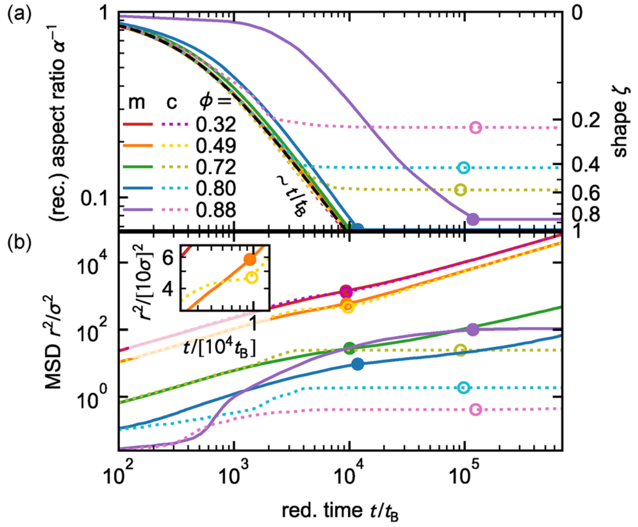

Fig. 6 Temporal evolution of (a) the shape parameter ζ and (b) the MSD [eqn (4)] for several packing fractions ϕ and both the morphing (m) and cascading (c) protocols. The disks and circles indicate the time when the protocol reaches the final shape and no shape updates are attempted beyond this time. The black dashed curve indicates the linear regime $\zeta \sim t/t_B$ that is obeyed at low packing fractions. The inset displays a zoom for packing fraction $\phi = 0.49$ when reaching the final shape. Colors and line styles are consistent with Fig. 2.

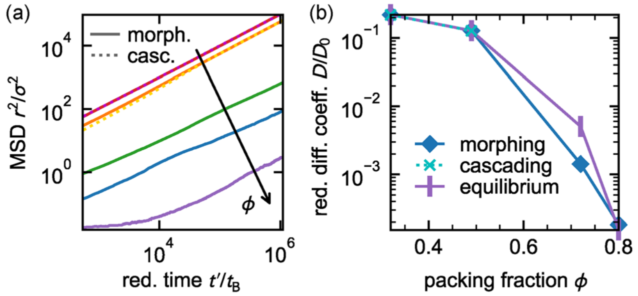

Fig. 7 Post-sweep diffusion behavior. (a) MSD based on eqn (4) as a function of the reduced time t'/t_B for hard rectangles with aspect ratio $\alpha = 15$ ($\zeta = 1$) following the morphing (solid) and cascading (dotted) protocol. Colors and line styles are consistent with Fig. 2. (b) Long-time reduced diffusion coefficient D/D_0 for hard rectangles (with aspect ratio $\alpha \simeq 15$) originating from the morphing protocol (blue) and cascading protocol (cyan). In the latter protocol, hard rectangles (with aspect ratio $\alpha \simeq 15$) are only obtained for low packing fractions $\phi < \phi_c \simeq 0.54$ (*cf.* inset in Fig. 2). As reference, we show the equilibrium values of D/D_0 (purple) for hard rectangles with aspect ratio $\alpha = 15$ that have been initialized at a high packing fraction in the smectic phase without undergoing a transformation process (*cf.* Fig. 5).

For the morphing protocol, we also observe a flattening of the MSD for the highest packing fraction $\phi = 0.88$ [Fig. 6(b)], apparently suggesting that the dynamics become arrested. To investigate the dynamics after finishing the shape protocol, we perform additional simulations without shape changes, for which we take the final sweep configurations as initial configurations. We calculate the MSD with respect to this reference frame ($\tau' = 0$) and recover normal diffusion in the long-time limit [Fig. 7(a)]. For low packing fractions ($\phi < \phi_c$), the MSDs of both protocols in Fig. 7(a) are in close accordance, *cf.* Fig. 5. For $\phi > \phi_c$ the MSDs are essentially flat for the cascading protocol and the corresponding diffusion coefficients vanish also in the continued simulations without shape changes. We conclude that for high packing fractions ($\phi > \phi_c$), the simulation path taken plays a fundamental role and – even for relatively long relaxation times $\Delta\tau \sim 10^8$ – the "memory" of the system does not forget its path. For instance, the diffusion coefficient D/D_0 for hard rectangles (aspect ratio $\alpha = 15$) clearly differs for $\phi > \phi_c$. This observation can be understood by taking into account that changing the shape can result in a metastable state that exhibits another phase than the actual equilibrium phase. Likewise, at $\phi = 0.72$, rod-like rectangles ($\alpha = 15$) self-assemble in a (uniaxial) nematic phase in equilibrium, whereas after morphing the system is in a metastable state, featuring a biaxial order. The higher value of D/D_0 in the former case is reasonable, because the nematic phase enhances parallel diffusion (along the director), where the rod-like particles can slide past each other. Obviously, this kind of movement is prevented in the biaxial order of the metastable state. Intriguingly, D/D_0 is in close accordance at $\phi = 0.80$ for rectangles ($\alpha = 15$), although the order depending on the path differs: we recapitulate that after morphing the system does not result in a smectic phase (as naively expected from Fig. 2), but rather remains in a biaxial metastable state.

3.3 Evolution of orientational order

To gain further insights into the ordering of particles during the shape sweep and the subsequent relaxation, we employ the two order parameters

$$\psi_\nu = \left\langle \left| \frac{1}{N} \sum_{k=1}^{N} e^{i\nu\theta_k} \right|^2 \right\rangle \tag{5}$$

with $\nu = 2{,}4$ and $0 \leq \psi_\nu \leq 1$ measuring orientational order. Their logical conjunction allows us to distinguish the different phases according to Table 1. The temporal evolution of the order parameters is shown in Fig. 8. Initially, for each pair of sweeps the order coincides as both protocols start from the same pre-relaxed system of squares. In accordance with our conclusions for the diffusion behavior, we find that the orientational order during both protocols qualitatively agrees for sweeps at low packing fraction ($\phi < \phi_c$), where the systems remain isotropic ($\psi_2 \simeq \psi_4 \simeq 0$) as in equilibrium (*cf.* Fig. 2 and SI[39]). Notably, the expected final nematic phase is absent during the cascading protocol and only manifests once the caging has vanished, whereas the emergence of this phase is already observed during the finalization of the morphing protocol. This observation is qualitatively rationalized by the lower degree of rotational symmetry of the cascading shapes. All sweeps at low packing fractions ($\phi < \phi_c$) exhibit the same orientational order during relaxation and reach the stable equilibrium state.[39]

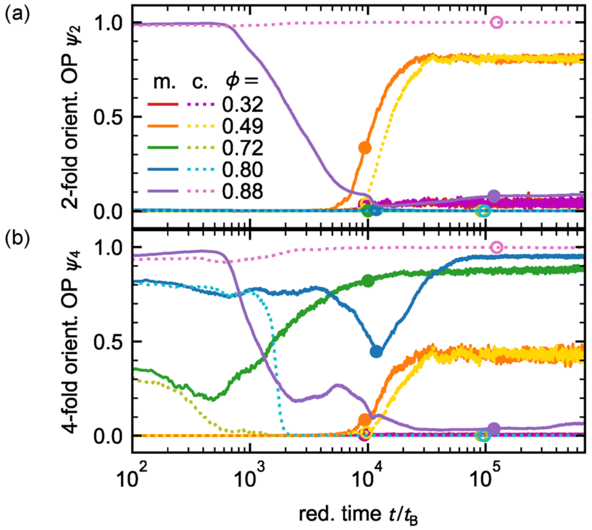

Fig. 8 Evolution in terms of reduced time t/t_B of the orientational order parameters (a) ψ_2 and (b) ψ_4 defined in eqn (5) following the evolution of the shape shown in Fig. 6(a).

Table 1 Idealized values of the ν-fold orientational order parameters ψ_ν [eqn (5)] characterizing the isotropic (I), tetratic (T), nematic (N) or smectic (S) phase. The actual equilibrium values for hard rectangles with various aspect ratios $\alpha \in$ (1,15] are summarized in the Supplemental Information[39]

Phase	ψ_4	ψ_2
I	0	0
T	1	0
N/S	1	1

At packing fraction $\phi = 0.72$, sweeps start in the tetratic phase and their ψ_4 signals diverge early ($t/t_B \sim 3 \times 10^2$). While there is still normal diffusion, the emerging non-rectangular shapes of the cascading protocol show an early replacement of the tetratic phase by the isotropic phase [*cf.* Fig. 3(a)]. The observed behavior during the morphing protocol is different, where ψ_4 essentially scans the equilibrium state point ($\alpha,\phi = 0.72$) values of rectangles with aspect ratio α.[39] In contrast to equilibrium, ψ_2 does not show any signal, *i.e.*, the expected final nematic order is absent and not reached even after long relaxation. Accordingly, the TN transition is suppressed, which can be interpreted as a further indicator for its discontinuous character as suggested in ref. 13. The sequence of snapshots in Fig. 9(a)–(c) illustrates the evolution into this final metastable state that exhibits a biaxial orientation order.

Qualitatively, increasing the packing fraction to $\phi = 0.80$ both protocols behave similarly to the previous case except for an effect occurring at the end of the morphing protocol: In contrast to the equilibrium expectation ($\psi_4 \simeq 1$[39]) the value of ψ_4 drops. However, it rises again and saturates towards its equilibrium value as soon as the shape transformation is accomplished. Interestingly, this temporal drop of ψ_4 occurs in the neighborhood of the equilibrium TS transition parameter range [*cf.* Fig. 2, 6(a) and 8(b)], which is also suppressed ($\psi_2 \simeq 0$) in favor of a metastable tetratic phase – in accordance with the strong hysteresis for the equilibrium TS transition discussed in ref. 13. A visual inspection of Fig. 9(d)–(f) reveals that the temporal drop of ψ_4 can be attributed to the emergence of defects, which exhibit the character of smectic domains that

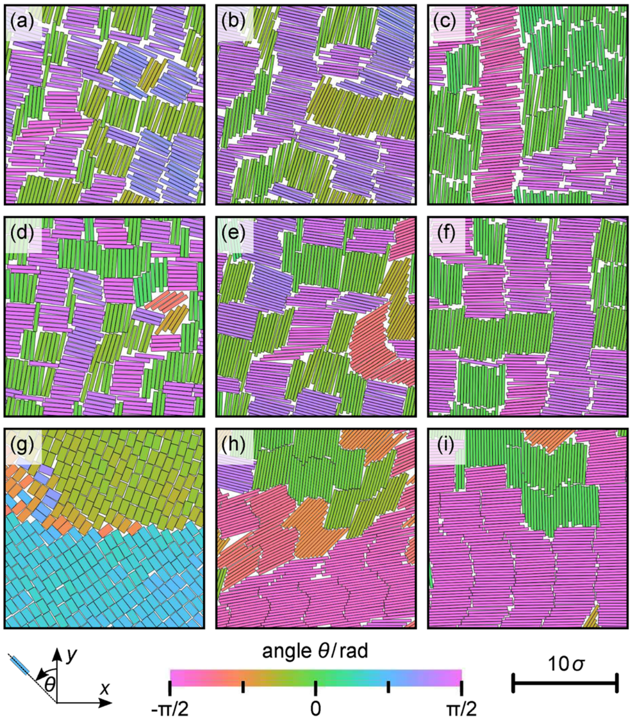

Fig. 9 Sequences of simulation snapshots (excerpts of the full system) showing the temporal evolution during the morphing protocol for the high packing fractions: (a)–(c) ϕ = 0.72 ($t/t_B \simeq 5.6 \times 10^3$, 1.0×10^4, 9.2×10^5; $\zeta \simeq 0.59$, 0.99, 1.00), (d)–(f) ϕ = 0.80 ($t/t_B \simeq 5.4 \times 10^3$, 1.2×10^4, 9.2×10^5; $\zeta \simeq 0.48$, 1.00, 1.00), and (g)–(i) ϕ = 0.88 ($t/t_B \simeq 5.0 \times 10^3$, 8.3×10^4, 9.9×10^5; $\zeta \simeq 0.05$, 1.00, 1.00).

align in the further progress according to the two favored directions of the overall biaxial order. We note that our finite-size analysis points to the tendency that this drop of ψ_4 becomes slightly weaker as the system size increases.[39]

Finally, starting from even more densely packed squares at ϕ = 0.88, the cascading protocol jams early and remains uniaxial [$\psi_2 \simeq \psi_4 \simeq 1$, *cf.* Fig. 3(c) and 8]. On the contrary, the morphing protocol succeeds in the transformation but shows a non-monotonic behavior at intermediate times before terminating at $\psi_2 \simeq \psi_4 \simeq 0$, which is the opposite of the equilibrium expectation ($\psi_2 \simeq \psi_4 \simeq 1$[39]). Thus, for the morphing protocol at ϕ = 0.88 neither a global uni- nor biaxial phase manifests, also not after a long relaxation. Fig. 9(g)–(i) suggest that interfaces are formed due to kinetic arrest between local packings alongside defects that lead to the emergence of competing local smectic clusters without a distinct global orientational order. It is conceivable that the defects serve as nucleation sites, which are frozen into a kinetically trapped state. Another technical aspect at high packing fractions is the non-commensurability (*i.e.*, an incompatible simulation box aspect ratio).

4 Conclusions

To conclude, we have numerically investigated the response of hard rectangles to dynamic shape changes. We compare two protocols for the same initial and final aspect ratio: (i) the simplified morphing protocol, whereby the aspect ratio of the rectangles is successively increased, and (ii) the cascading protocol mimicking the experimental process more closely. For the cascading protocol, we find a transition between two regimes: For low packing fractions ($\phi < \phi_c$ with $\phi_c \simeq 0.54$) the dynamics and ordering during the shape change and in the stationary regime are in close agreement and recover equilibrium properties. For high packing fractions ($\phi > \phi_c$) the evolution of the shape cannot proceed to the target shape and the system becomes dynamically arrested as evident in the mean-square displacement, which levels off to a plateau. Since the morphing protocol (going through a sequence of space-filling rectangles with increasing aspect ratio) proceeds without dynamic arrest even for the highest packing fraction (ϕ = 0.88), we attribute the observed jamming of particles to the non-space-filling nature of the cascading shapes effectively decreasing the available area. This explanation is corroborated through introducing an effective packing fraction, and we observe that reaching unity coincides with the onset of jamming. For the morphing protocol the tetratic phase becomes predominant both during the evolution and in the stationary regime: In particular, a shape sweep starting in the tetratic phase and terminating within the phase boundaries of the nematic phase (ϕ = 0.72) remains tetratic even after a long relaxation of $\Delta\tau \simeq 10^8$ MC time steps. Moreover, we find that a sweep (ϕ = 0.80) that crosses the tetratic-smectic transition in the phase diagram of hard rectangles does not result in the smectic phase, but rather in a metastable tetratic phase and supports the identification of the tetratic-smectic transition as discontinuous in ref. 13.

In the quest for functional and adaptive soft materials and their autonomous assembly, designing programmable and dynamically changing interactions has moved into the focus, *e.g.* through exploiting allosteric transitions.[52,53] For (almost) hard particles, adaptive interactions can be achieved through adjusting the particle shape.[16] Moreover, understanding the response to dynamic changes offers the opportunity to go beyond stable equilibrium structures and to access "polymorphs" through metastable states. Our numerical study is a first step towards understanding how such shape changes might be exploited to design and access long-lived metastable collective states in (effectively) hard particles based on the knowledge of the underlying equilibrium phase diagram and the nature of transitions. While we have looked at the limit of quasi-static protocols (as appropriate for DNA nanostructures), the rate with which the shape change proceeds is another control parameter to be explored in the future.

Conflicts of interest

There are no conflicts of interest to declare.

Data availability

Simulations were performed using HOOMD-blue (https://github.com/glotzerlab/hoomd-blue/releases/tag/v4.8.2). The processed simulation data are available at https://doi.org/10.18419/DARUS-5377.

Supplementary information (SI) is available. See DOI: https://doi.org/10.1039/d6sm00037a.

Acknowledgements

Simulations have been performed using the bwHPC infrastructure (clusters BinAC and BinAC2) supported by the state of Baden-Württemberg and the Deutsche Forschungsgemeinschaft (DFG) through projects INST 37/935-1 and 37/1159-1 FUGG. In addition, we gratefully acknowledge support through SimTech (University of Stuttgart and DFG project no. 390740016 – EXC 2075) and the GRK 2516 (DFG project No. 405552959).

References

1 C. P. Royall, P. Charbonneau, M. Dijkstra, J. Russo, F. Smallenburg, T. Speck and C. Valeriani, Colloidal hard spheres: Triumphs, challenges, and mysteries, *Rev. Mod. Phys.*, 2024, **96**, 045003.

2 S. Sacanna, M. Korpics, K. Rodriguez, L. Colón-Meléndez, S.-H. Kim, D. J. Pine and G.-R. Yi, Shaping colloids for self-assembly, *Nat. Commun.*, 2013, **4**, 1688.

3 C. L. Bassani, G. Van Anders, U. Banin, D. Baranov, Q. Chen, M. Dijkstra, M. S. Dimitriyev, E. Efrati, J. Faraudo, O. Gang, N. Gaston, R. Golestanian, G. I. Guerrero-Garcia, M. Gruenwald, A. Haji-Akbari, M. Ibáñez, M. Karg, T. Kraus, B. Lee, R. C. Van Lehn, R. J. Macfarlane, B. M. Mognetti, A. Nikoubashman, S. Osat, O. V. Prezhdo, G. M. Rotskoff, L. Saiz, A.-C. Shi, S. Skrabalak, I. I. Smalyukh, M. Tagliazucchi, D. V. Talapin, A. V. Tkachenko, S. Tretiak, D. Vaknin, A. Widmer-Cooper, G. C. L. Wong, X. Ye, S. Zhou, E. Rabani, M. Engel and A. Travesset, Nanocrystal Assemblies: Current Advances and Open Problems, *ACS Nano*, 2024, **18**, 14791.

4 P. F. Damasceno, M. Engel and S. C. Glotzer, Predictive Self-Assembly of Polyhedra into Complex Structures, *Science*, 2012, **337**, 453.

5 A. S. Keys, C. R. Iacovella and S. C. Glotzer, Characterizing complex particle morphologies through shape matching: Descriptors, applications, and algorithms, *J. Comput. Phys.*, 2011, **230**, 6438.

6 R. Wittkowski and H. Löwen, Dynamical density functional theory for colloidal particles with arbitrary shape, *Mol. Phys.*, 2011, **109**, 2935.

7 T. Vo and S. C. Glotzer, A theory of entropic bonding, *Proc. Natl. Acad. Sci. U. S. A.*, 2022, **119**, e2116414119.

8 J. A. Anderson, J. Antonaglia, J. A. Millan, M. Engel and S. C. Glotzer, Shape and Symmetry Determine Two-Dimensional Melting Transitions of Hard Regular Polygons, *Phys. Rev. X*, 2017, **7**, 021001.

9 S. Mizani, M. Oettel, P. Gurin and S. Varga, Competition between shape anisotropy and deformation in the ordering and close packing properties of quasi-one-dimensional hard superellipse fluids, *Phys. Rev. E*, 2025, **111**, 064121.

10 E. P. Bernard and W. Krauth, Two-Step Melting in Two Dimensions: First-Order Liquid-Hexatic Transition, *Phys. Rev. Lett.*, 2011, **107**, 155704.

11 M. Engel, J. A. Anderson, S. C. Glotzer, M. Isobe, E. P. Bernard and W. Krauth, Hard-disk equation of state: First-order liquid-hexatic transition in two dimensions with three simulation methods, *Phys. Rev. E*, 2013, **87**, 042134.

12 S. C. Kapfer and W. Krauth, Two-Dimensional Melting: From Liquid-Hexatic Coexistence to Continuous Transitions, *Phys. Rev. Lett.*, 2015, **114**, 035702.

13 D. Dertli and T. Speck, In pursuit of the tetratic phase in hard rectangles, *Phys. Rev. Res.*, 2025, **7**, L012034.

14 Y. Sun, J. S. Evans, T. Lee, B. Senyuk, P. Keller, S. He and I. I. Smalyukh, Optical manipulation of shape-morphing elastomeric liquid crystal microparticles doped with gold nanocrystals, *Appl. Phys. Lett.*, 2012, **100**, 241901.

15 E. Epstein, J. Yoon, A. Madhukar, K. J. Hsia and P. V. Braun, Colloidal Particles that Rapidly Change Shape via Elastic Instabilities, *Small*, 2015, **11**, 6051.

16 N. Tanjeem, M. B. Minnis, R. C. Hayward and C. W. Shields, Shape-Changing Particles: From Materials Design and Mechanisms to Implementation, *Adv. Mater.*, 2022, **34**, 2105758.

17 P. Zhan, A. Peil, Q. Jiang, D. Wang, S. Mousavi, Q. Xiong, Q. Shen, Y. Shang, B. Ding, C. Lin, Y. Ke and N. Liu, Recent Advances in DNA Origami-Engineered Nanomaterials and Applications, *Chem. Rev.*, 2023, **123**, 3976.

18 P. W. K. Rothemund, Folding DNA to create nanoscale shapes and patterns, *Nature*, 2006, **440**, 297.

19 H. Dietz, S. M. Douglas and W. M. Shih, Folding DNA into Twisted and Curved Nanoscale Shapes, *Science*, 2009, **325**, 725.

20 F. Hong, F. Zhang, Y. Liu and H. Yan, DNA Origami: Scaffolds for Creating Higher Order Structures, *Chem. Rev.*, 2017, **117**, 12584.

21 M. Endo, Y. Yang and H. Sugiyama, DNA origami technology for biomaterials applications, *Biomater. Sci.*, 2013, **1**, 347.

22 Y. Sun, J. Sun, M. Xiao, W. Lai, L. Li, C. Fan and H. Pei, DNA origami-based artificial antigen-presenting cells for adoptive T cell therapy, *Sci. Adv.*, 2022, **8**, eadd1106.

23 S. He, T. Fan, Y. Wang, C. Wei and J. Hu, Recent Advances in DNA Nanostructure-enabled Drug Delivery, *ChemNanoMat*, 2023, **9**, e202200459.

24 Y. Zhang, X. Tian, Z. Wang, H. Wang, F. Liu, Q. Long and S. Jiang, Advanced applications of DNA nanostructures dominated by DNA origami in antitumor drug delivery, *Front. Mol. Biosci.*, 2023, **10**, 1239952.

25 M. Safarkhani, S. Ahmadi, H. Ipakchi, M. R. Saeb, P. Makvandi, M. Ebrahimi Warkiani, N. Rabiee and Y. Huh, Advancements in Aptamer-Driven DNA Nanostructures for Precision Drug Delivery, *Adv. Sci.*, 2024, **11**, 2401617.

26 L. Ding, B. Liu, A. Peil, S. Fan, J. Chao and N. Liu, DNA-Directed Assembly of Photonic Nanomaterials for Diagnostic and Therapeutic Applications, *Adv. Mater.*, 2025, 2500086.

27 A. Khmelinskaia, H. G. Franquelim, R. Yaadav, E. P. Petrov and P. Schwille, Membrane-Mediated Self-Organization of Rod-Like DNA Origami on Supported Lipid Bilayers, *Adv. Mater. Interfaces*, 2021, **8**, 2101094.

28 S. Fan, S. Wang, L. Ding, T. Speck, H. Yan, S. Nussberger and N. Liu, Morphology remodelling and membrane channel formation in synthetic cells via reconfigurable DNA nanorafts, *Nat. Mater.*, 2025, **24**, 278.

29 D. Y. Zhang and G. Seelig, Dynamic DNA nanotechnology using strand-displacement reactions, *Nat. Chem.*, 2011, **3**, 103.

30 J. Song, Z. Li, P. Wang, T. Meyer, C. Mao and Y. Ke, Reconfiguration of DNA molecular arrays driven by information relay, *Science*, 2017, **357**, eaan3377.

31 D. Wang, L. Yu, B. Ji, S. Chang, J. Song and Y. Ke, Programming the Curvatures in Reconfigurable DNA Domino Origami by Using Asymmetric Units, *Nano Lett.*, 2020, **20**, 8236.

32 M. Kim, C. Lee, K. Jeon, J. Y. Lee, Y.-J. Kim, J. G. Lee, H. Kim, M. Cho and D.-N. Kim, Harnessing a paper-folding mechanism for reconfigurable DNA origami, *Nature*, 2023, **619**, 78.

33 S. Seo, A. Swett, M. R. Kesama, A. Madhvacharyula, R. Li, Y. Du, M. Eder, F. C. Simmel and J. H. Choi, A Nanoscale Jitterbug Transformer from DNA, 2025.

34 D. Frenkel and B. Smit, *Understanding Molecular Simulation: From Algorithms to Applications*, Elsevier, 2023.

35 J. A. Anderson, C. D. Lorenz and A. Travesset, General purpose molecular dynamics simulations fully implemented on graphics processing units, *J. Comput. Phys.*, 2008, **227**, 5342.

36 J. Glaser, T. D. Nguyen, J. A. Anderson, P. Lui, F. Spiga, J. A. Millan, D. C. Morse and S. C. Glotzer, Strong scaling of general-purpose molecular dynamics simulations on GPUs, *Comput. Phys. Commun.*, 2015, **192**, 97.

37 J. A. Anderson, M. Eric Irrgang and S. C. Glotzer, Scalable Metropolis Monte Carlo for simulation of hard shapes, *Comput. Phys. Commun.*, 2016, **204**, 21.

38 J. A. Anderson, J. Glaser and S. C. Glotzer, HOOMD-blue: A Python package for high-performance molecular dynamics and hard particle Monte Carlo simulations, *Comput. Mater. Sci.*, 2020, **173**, 109363.

39 Supplemental information, supplemental material at https://doi.org/10.1039/d6sm00037a containing additional information on the simulations and calculations.

40 A. Patti and A. Cuetos, Brownian dynamics and dynamic Monte Carlo simulations of isotropic and liquid crystal phases of anisotropic colloidal particles: A comparative study, *Phys. Rev. E*, 2012, **86**, 011403.

41 A. Cuetos and A. Patti, Equivalence of Brownian dynamics and dynamic Monte Carlo simulations in multicomponent colloidal suspensions, *Phys. Rev. E*, 2015, **92**, 022302.

42 R. L. Jack, I. R. Thompson and P. Sollich, Hyperuniformity and Phase Separation in Biased Ensembles of Trajectories for Diffusive Systems, *Phys. Rev. Lett.*, 2015, **114**, 060601.

43 D. Corbett, A. Cuetos, M. Dennison and A. Patti, Dynamic Monte Carlo algorithm for out-of-equilibrium processes in colloidal dispersions, *Phys. Chem. Chem. Phys.*, 2018, **20**, 15118.

44 N. Morillo, A. Patti and A. Cuetos, Brownian dynamics simulations of oblate and prolate colloidal particles in nematic liquid crystals, *J. Chem. Phys.*, 2019, **150**, 204905.

45 D. J. Kraft, R. Wittkowski, B. Ten Hagen, K. V. Edmond, D. J. Pine and H. Löwen, Brownian motion and the hydrodynamic friction tensor for colloidal particles of complex shape, *Phys. Rev. E*, 2013, **88**, 050301.

46 J. G. Hernández-Cifre, R. Rodríguez-Schmidt, C. M. Almagro-Gómez and J. García De La Torre, Calculation of the friction, diffusion and sedimentation coefficients of nanoplatelets of arbitrary shape, *Polymer*, 2022, **262**, 125467.

47 J. García De La Torre, G. Del Rio Echenique and A. Ortega, Improved Calculation of Rotational Diffusion and Intrinsic Viscosity of Bead Models for Macromolecules and Nanoparticles, *J. Phys. Chem. B*, 2007, **111**, 955.

48 J. Garcia De La Torre, S. Navarro, M. Lopez Martinez, F. Diaz and J. Lopez Cascales, HYDRO: A computer program for the prediction of hydrodynamic properties of macromolecules, *Biophys. J.*, 1994, **67**, 530.

49 J. G. De La Torre and V. A. Bloomfield, Hydrodynamic properties of complex, rigid, biological macromolecules: Theory and applications, *Quart. Rev. Biophys.*, 1981, **14**, 81.

50 B. Carrasco and J. García De La Torre, Hydrodynamic Properties of Rigid Particles: Comparison of Different Modeling and Computational Procedures, *Biophys. J.*, 1999, **76**, 3044.

51 V. Ramasubramani, B. D. Dice, E. S. Harper, M. P. Spellings, J. A. Anderson and S. C. Glotzer, Freud: A software suite for high throughput analysis of particle simulation data, *Comput. Phys. Commun.*, 2020, **254**, 107275.

52 G. R. Lazaro and M. F. Hagan, Allosteric Control of Icosahedral Capsid Assembly, *J. Phys. Chem. B*, 2016, **120**, 6306.

53 J. Metson, Designing complex behaviors using transition-based allosteric self-assembly, *Phys. Rev. Res.*, 2025, **7**, 033044.